

Ekman-Inertial Instability

By

Nicolas Grisouard (nicolas.grisouard@utoronto.ca) and

Varvara E. Zemskova (barbara.zemskova@utoronto.ca)

*University of Toronto, Department of Physics, 60 St. George Street, Toronto ON M5S
1A7, Canada*

This paper is a non-peer reviewed preprint submitted to EarthArXiv. It was submitted to Physical Review Fluids on 26 June 2020 and is currently undergoing peer review. Should it be accepted, the final version of this manuscript will be available via the '*Peer-review Publication DOI*' link on the right-hand-side of this webpage. Please feel free to contact any of the authors.

Ekman-Inertial Instability

Nicolas Grisouard^{*} and Varvara E. Zemskova

University of Toronto, Department of Physics, 60 St. George Street, Toronto ON M5S 1A7, Canada

(Dated: June 26, 2020)

We report on an instability, arising in sub-surface, laterally-sheared flows in rotation. When the lateral shear of a horizontal flow in geostrophic balance is of opposite sign as the Coriolis parameter, and exceeds it in magnitude, embedded perturbations are subjected to inertial instability, albeit modified by viscosity. When the perturbation arises from the surface of the fluid, the initial response is akin to a Stokes problem, with an initial flow aligned with the initial perturbation. Perturbation then grows quasi-inertially, rotation deflecting the velocity vector, which adopts a well-defined angle with the mean flow. While the perturbation initially grows super-inertially, the growth rate then becomes sub-inertial, eventually tending back to the inertial value. The same process repeats downward as time progresses. Ekman-inertial transport aligns with the asymptotic orientation of the flow, and grows exactly inertially with time, once the initial instants have passed. Because of the strongly super-inertial initial growth rate, this instability might compete favorably against other instabilities arising in ocean fronts.

I. INTRODUCTION

When wind blows over the ocean surface over long periods of time, momentum diffuses down in a very different manner from Stokes' first problem. Instead, the Coriolis acceleration balances downward diffusion of momentum to form Ekman spirals [1]. According to its simplest description [2], horizontal velocity at the surface forms a 45°-angle with the direction of the wind, and within the Ekman layer (hereafter referred to as EL), spirals down to zero over a depth $O(\sqrt{2\nu/f})$, where ν is the kinematic viscosity (hereafter “viscosity”), in practice the vertical eddy viscosity, and f is the Coriolis parameter. In spite of its simplicity and notorious difficulty to directly observe in the ocean, this solution has allowed some significant advances in our understanding of ocean dynamics. For example, the predicted cumulative mass transport of ELs provides a relatively accurate explanation of how winds set up ocean gyres [1, 3, and references therein]. Since then, Ekman layer theory has been amended to include weak vorticity effects [4–6], or variability of the wind and eddy diffusivity both in space [7] and time [8].

EL theory has seen a renewed interest in the context of submesoscale studies [9, 10]. Submesoscale flows are defined by a vertical vorticity field $\zeta = (\nabla \times \mathbf{v}) \cdot \hat{\mathbf{z}}$ with magnitude comparable to the planetary vorticity f , i.e., Rossby number of order unity ($\text{Ro} = \zeta/f = O(1)$). [11] Near the ocean surface, submesoscale flows and their associated vertical velocities could be important for ecosystems [12–14], atmosphere-ocean exchanges [15, 16], or as a kinetic energy sink that could help, closing the energy budget of the ocean [10, 17]. Recent studies have expanded our understanding of submesoscale ELs and their impacts by incorporating interactions with $\text{Ro} = O(1)$ vortical flows [3], surface waves and Langmuir circulation [18], and modifications due to baroclinic pressure torques [15, 19, 20].

In the present study, our goal is to contribute to this effort by describing an instability, hereafter referred to as “Ekman-Inertial Instability” (EII). It can be seen as the unstable counterpart of an EL that occurs in anticyclonic flows for which $\text{Ro} < -1$. Such flows can undergo inertial instability (InI), in which a particle slightly displaced across a geostrophic jet will find itself in a region where the imbalance between ambient pressure gradient and the Coriolis force tends to amplify its displacement [21, 22]. The main features of InI are well-described by linear stability analysis, i.e., by the growth of a plane wave-like mode at a rate of $f\sqrt{-1 - \text{Ro}}$ in the inviscid limit, constant in time and space.

EII, on the other hand, originates from a disturbance in the wind stress at the surface of the ocean, and the vertical extent over which it impacts the fluid increases downward due to viscous stresses, eventually following a typical $\sqrt{\nu t}$ scaling. In a first phase, which we will refer to as “viscous-inertial peeling”, tangential viscous stresses act to set the fluid in motion much faster than the expected exponential growth of InI. Past this initial phase, the flow keeps accelerating, akin to InI, but less so due to the downward diffusion of momentum by viscosity. Originating at the surface, these processes repeat at later times at greater depths.

In the next section, we derive the expressions of the velocity field under EII, followed in §III by a description of how EII physically manifests itself. In §IV, we discuss how EII would insert itself in the dynamical landscape of an unstable front, before offering a summary and conclusions in §V.

II. MATHEMATICAL DESCRIPTION

We present here the solution for the most idealized version of EII. We mirror this derivation with its “stable” counterpart, i.e., the establishment of an EL accompanied by near-inertial oscillations, in the appendix.

^{*} nicolas.grisouard@utoronto.ca

A. Velocity

We assume an initial velocity field $\bar{\mathbf{v}} = \bar{v}\hat{\mathbf{y}}$ in an $(\hat{\mathbf{x}}, \hat{\mathbf{y}}, \hat{\mathbf{z}})$ direct Cartesian coordinate system, with $\hat{\mathbf{z}}$ pointing vertically upward. The current is in geostrophic balance, i.e., $\rho f\bar{\mathbf{v}} = \bar{p}_y$, where \bar{p} is the geostrophic pressure field, ρ the mass density we assume constant, and a subscript denoting a partial derivative. In sub-surface currents, the velocity varies in the across-jet direction, which defines a local Rossby number

$$\text{Ro} = \bar{v}_x/f. \quad (1)$$

We treat Ro as a constant: a strong simplification in the submesoscale regime, but one that captures the essential physics of EII. We refer to the deviations from $\bar{\mathbf{v}}\hat{\mathbf{y}}$ as (u, v, w) . Like in ELs and InI, a constant Ro allows us to ignore all horizontal derivatives. From incompressibility and a top rigid lid, $w \equiv 0$, and the equations of motion reduce to

$$u_t - fv = \nu u_{zz} \quad \text{and} \quad v_t + (1 + \text{Ro})fu = \nu v_{zz}. \quad (2)$$

EII starts with a change in wind conditions at the surface at $t = 0$. The surface wind stress goes from a constant value T_I^y that matches the initial interior viscous stress $\rho\nu\bar{v}_z|_{z=0}$, and starts evolving as $T^y(t)$. The translation for v is that for $t \leq 0$, $v_z|_{z=0} = 0$ and for $t > 0$,

$$v_z|_{z=0} = a(t) = [T^y(t) - T_I^y]/(\nu\rho). \quad (3)$$

EL boundary conditions close the system, i.e.,

$$u_z|_{z=0} = 0 \quad \text{and} \quad \lim_{z \rightarrow -\infty} (u, v) = 0. \quad (4)$$

In order to decouple eqns. (2), we introduce

$$U = u + v/\alpha \quad \text{and} \quad V = -u + v/\alpha, \quad (5)$$

with $\alpha^2 = -1 - \text{Ro}$. In scaled coordinates

$$\tau = Ft \quad \text{and} \quad Z = z/\delta, \quad (6)$$

where $F = \alpha f$ and $\delta = \sqrt{2\nu/F}$, eqns. (2) become

$$U_\tau - U = U_{ZZ}/2 \quad \text{and} \quad V_\tau + V = V_{ZZ}/2. \quad (7)$$

Solving for $U^\dagger = Ue^{-\tau}$ and $V^\ddagger = Ve^\tau$ turns eqns. (7) into mere diffusion equations, e.g.,

$$2U_\tau^\dagger = U_{ZZ}^\dagger \quad \text{and} \quad U_\tau^\dagger|_{Z=0} = A(\tau)e^{-\tau}, \quad (8)$$

with $A(\tau) = a(\tau)\delta/\alpha$, together with boundary conditions (4). Note that we could include a perturbation in u_z at the surface as well in $A(\tau)$ with no loss of generality. The solution to this system is

$$U^\dagger = \int_0^\tau \frac{A(\tau')e^{-\tau'}}{\sqrt{2\pi(\tau - \tau')}} \exp\left(-\frac{Z^2}{2(\tau - \tau')}\right) d\tau'. \quad (9)$$

After multiplying with e^τ and the change of variables $\theta \mapsto \tau - \tau'$,

$$U = \int_0^\tau \frac{A(\tau - \theta)}{\sqrt{2\pi\theta}} \exp\left(\theta - \frac{Z^2}{2\theta}\right) d\theta. \quad (10)$$

A similar derivation for V yields

$$V = \int_0^\tau \frac{A(\tau - \theta)}{\sqrt{2\pi\theta}} \exp\left(-\theta - \frac{Z^2}{2\theta}\right) d\theta. \quad (11)$$

B. Validation strategy

To independently validate our findings, we solve equations (2)–(4) in the case of an abrupt change in boundary conditions (constant a and A) with the spectral code Dedalus (23) (24). The depth of our domain is 15δ , and we use 256 Chebyshev modes. We integrate the equations over $15/F$, which is long enough to see EII mature, but short enough that it does not reach the bottom of the domain, in agreement with the condition at infinity in eqns. (4). Because the one-dimensional equations (2) are linear, Dedalus integrates them implicitly in time with a 4th-order Runge-Kutta scheme. At the start of the simulation, u and v vary more strongly, and we progressively decrease the time step Δt following

$$\Delta t = \Delta t_m + (\Delta t_M - \Delta t_m)(1 - e^{-Ft}), \quad (12)$$

with $F\Delta t_m = 10^{-5}$ and $F\Delta t_M = 10^{-2}$.

Simulations shown here are seeded with noise, meaning that EII and InI compete. However, noise-free simulations (not shown) behave virtually identically. As expected from linear calculations, outcomes of numerical simulations and analytical solutions are practically indistinguishable. We present both below for the abrupt wind change case.

C. Solution following an abrupt change in wind

We now focus on the case when wind changes abruptly, i.e., for constant $A(\tau) = A_0$. We numerically tested moderate departures from this case, e.g., exponential approach to different, constant wind stress values over time scales similar to $1/F$ or shorter and found qualitatively and quantitatively similar behavior to the abrupt change case. Should the wind evolve over longer time scales, EII would likely initiate and saturate before said time scales have time to impart their signature on the flow.

Under this condition, eqn. (10) can be cast in the following closed forms

$$U = \frac{A_0}{\sqrt{2}} \Im \left[e^{Zi\sqrt{2}} \text{erfc} \left(-i\sqrt{\tau} - \frac{Z}{\sqrt{2\tau}} \right) \right] \quad (13a)$$

$$= \frac{A_0}{\sqrt{2}} e^{\tau - Z^2/(2\tau)} \Im \left[\mathcal{W} \left(\sqrt{\tau} + \frac{iZ}{\sqrt{2\tau}} \right) \right], \quad (13b)$$

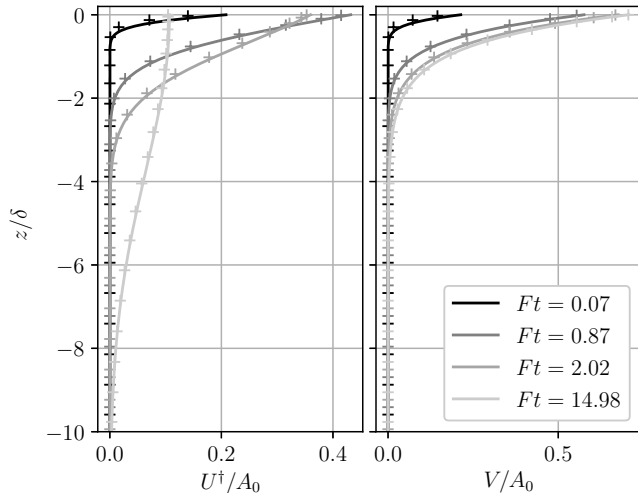


FIG. 1. Evolution of the profiles of U^\dagger and V , after an abrupt change in boundary conditions. Solid lines: analytical solutions derived in §III C; crosses: independent numerical integration of eqns. (2), described in §II B. We only display one cross every eight grid points.

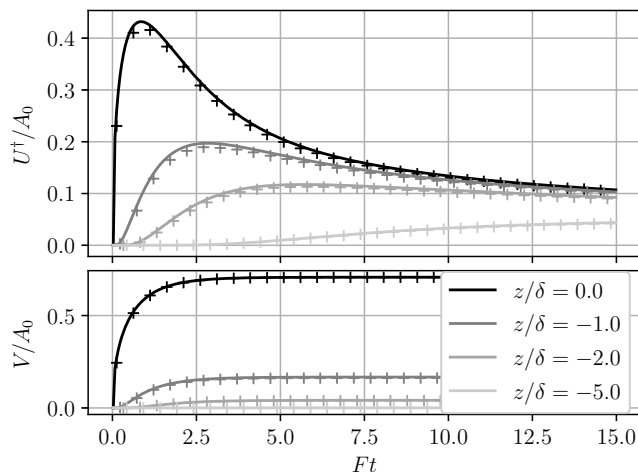


FIG. 2. Same as fig. 1 presented as time series at a few depths. We only display one cross every ten time steps.

where erfc is the complementary error function, \Im denotes the imaginary part and \mathcal{W} is the Faddeeva function

$$\forall \xi \in \mathbb{C}, \quad \mathcal{W}(\xi) = e^{-\xi^2} \text{erfc}(-i\xi).$$

We plot U^\dagger corresponding to this solution in figs. 1 (left panel) and 2 (top panel).

Eqn. (13b) highlights the long-term behavior of the solution. First, e^τ is the only factor that exhibits a persistently growing behavior, while the rest, namely, U^\dagger , is bounded at all times. In fact, U grows indefinitely, albeit at a rate that keeps evolving, which we will discuss in §II D. Second, for $\tau \gg 1$, $\mathcal{W}(\dots) \approx \mathcal{W}(\sqrt{\tau})$, and the Z -dependence mostly manifest itself in the $e^{-Z^2/(2\tau)}$

factor. Therefore, the bell-shaped profile of U^\dagger found at $Ft \approx 15$ in fig. 1 is a weakly-modulated Gaussian, whose vertical extent scales as $\sqrt{\nu t}$ in dimensional coordinates.

Similarly, eqn. (11) becomes

$$V = \frac{A_0}{2\sqrt{2}} \left[e^{Z\sqrt{2}} \text{erfc} \left(-\sqrt{\tau} - \frac{Z}{\sqrt{2\tau}} \right) - e^{-Z\sqrt{2}} \text{erfc} \left(\sqrt{\tau} - \frac{Z}{\sqrt{2\tau}} \right) \right], \quad (14)$$

which we plot in figs. 1 (right panel) and 2 (bottom panel). Contrary to U , the error functions above have real arguments, bounding V at all times and depths. In particular, for $\tau \gg 1$, $V \approx A_0/\sqrt{2}e^{Z\sqrt{2}}$ and does not extend deeper than $O(\delta)$.

Figs. 1 and 2 show that EII is most pronounced at the surface. There, eqns. (13) have simple analytical expressions, namely

$$U|_{Z=0} = \frac{A_0}{\sqrt{2}} \text{erfi}(\sqrt{\tau}) = \sqrt{\frac{2}{\pi}} A_0 e^\tau D(\sqrt{\tau}), \quad (15a)$$

$$V|_{Z=0} = \frac{A_0}{\sqrt{2}} \text{erf}(\sqrt{\tau}), \quad (15b)$$

where erfi is the imaginary error function and

$$\forall \xi \in \mathbb{R}, \quad D(\xi) = \frac{\sqrt{\pi}}{2} e^{-\xi^2} \text{erfi}(\xi)$$

is the Dawson integral. It is bounded, with $D(\sqrt{\tau}) \approx \sqrt{\tau}$ for $\tau \ll 1$, then going through a maximum at $\tau \approx 0.92$, before decaying monotonically to zero, eventually as $1/(2\sqrt{\tau})$.

D. Growth rate

The general expression for the growth rate of U is

$$\sigma_U(t, Z) = \frac{1}{U} \frac{\partial U}{\partial t} = F + \frac{1}{U^\dagger} \frac{\partial U^\dagger}{\partial t}. \quad (16)$$

We hereafter refer to periods of time when $\sigma_U > F$ ($\sigma_U < F$) as “super-inertial” (“sub-inertial”), in reference to the growth rate of inviscid InI.

The growth rates of U and V can be readily obtained from eqns. (10)–(11) and the Leibniz integral rule. We explicitly plot σ_U in the case of a sudden wind change in fig. 3. In accordance with eqn. (16), periods of U^\dagger increasing (decreasing) in fig. 2 correspond to phases over which U grows super-inertially (sub-inertially). Qualitatively, the growth rate behaves similarly at all depths. Thus, we focus on the surface behavior, which also has the strongest impact on the dynamics of a front. There,

$$\sigma_0 = \sigma_U|_{Z=0} = [2\sqrt{\tau} D(\sqrt{\tau})]^{-1}, \quad (17)$$

which we can break down following the discussion at the end of §III C. That is, for $\tau \ll 1$, $\sigma_0 \approx 1/(2\tau)$, and the

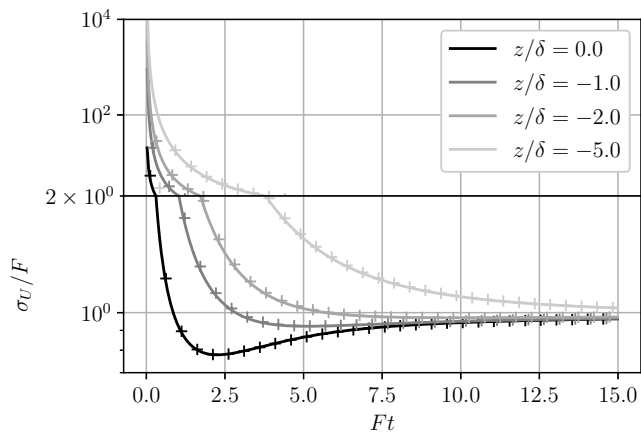


FIG. 3. Same as fig. 2 for growth rates σ_U . Note the change in vertical log scale at $\sigma_U = 2F$, curves would appear infinitely differentiable otherwise.

growth rate goes from infinity to unity within a duration $\tau \approx 0.854$. It then decreases and reaches a minimum of $\sigma_0 \approx 0.778F$ at $\tau \approx 2.26$. The growth rate then monotonically increases and asymptotically tends to F .

At depth, the flow qualitatively goes through the same series of steps, with quantitative differences. As Z decreases, the initial growth rate increases in absolute value due to lower values of U . It reaches the $\sigma_U = F$ mark, then its minimum value, which is closer to F at greater depth, at later times.

III. INSTABILITY DYNAMICS

This section presents a more qualitative description of EII, namely, the physical mechanisms involved, the morphology of the induced flow, and the implication on mass transport.

A. Dynamics through the lens of energetics

The individual mechanisms involved in EII can be better traced by investigating their energetic signatures. From eqns. (2), the evolution equation of the kinetic energy density of the flow $K = (u^2 + v^2)/2$ is

$$K_t = -LSP - \Phi_z - \epsilon, \quad (18)$$

where $LSP = \text{Rof}uv$ stands for Lateral Shear Production, i.e., the transfer of kinetic energy from perturbations to the mean shear (negative here); $\Phi = -\nu K_z$, the viscous diffusive flux of kinetic energy; and $\epsilon = \nu(u_z^2 + v_z^2)$, the irreversible dissipation.

Fig. (4) shows that Φ_z plays a role that depends on the phase of EII. In the first phase, which we refer to as “Viscous-Inertial Peeling” (VIP), $-\Phi_z$ is the dominant energy source at the leading edge of the instability,

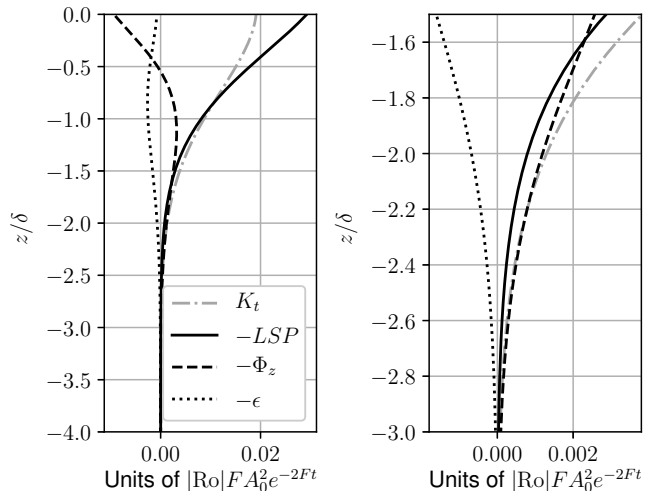


FIG. 4. Kinetic energy budget at $Ft = 2$ (cf. eqn. 18). The right-hand-side panel is a magnification of the left-hand-side panel around the edge of the EII propagation. These plots are from the numerical simulation.

setting the fluid in motion, with $-LSP$ being the secondary energy source. This phase (fig. 4 right panel) coincides with the super-inertial growth we described in §III D. Near the surface, it lasts $O(F^{-1})$, too short for rotation to influence the dynamics significantly. VIP is therefore a Rayleigh-like problem, rotation acting as a perturbation.

After the instability front has passed however (fig. 4 $z/\delta > -1.5$), $-LSP$ becomes the dominant source of energy, as in InI, and $-\Phi_z$ acts to reduce the growth of the instability. Physically, rotation is now acting and the flow set in motion during VIP is inertially unstable, a phase we call “Inertial-Viscous Instability” (InVI). Upper layers of the fluid have begun going unstable earlier than lower layers, and their velocity proceeds to grow quasi-exponentially. The result is a persistent horizontal momentum imbalance between upper and lower layers, which viscosity diffuses downward. InVI therefore behaves like a viscously-dragged InI. As time progresses, EII behaves more and more like inviscid InI: relatively speaking, the vertical gradients diminish (see fig. 1), Φ_z becomes less important, and the growth rate approaches F .

B. Hodograph

EII induces a peculiar velocity field, with some features reminiscent of the Ekman spiral (see fig. 5), with a caveat that we address in the next paragraph. During the early phases of VIP and near the surface, $e^{\pm\tau} \approx 1$ and eqns. (10)–(11) show that U and V both initially grow at similar rates. Rotation is not acting yet, and the motion is along the original wind perturbation direction (fig. 5, left panel). Later, as VIP transitions into

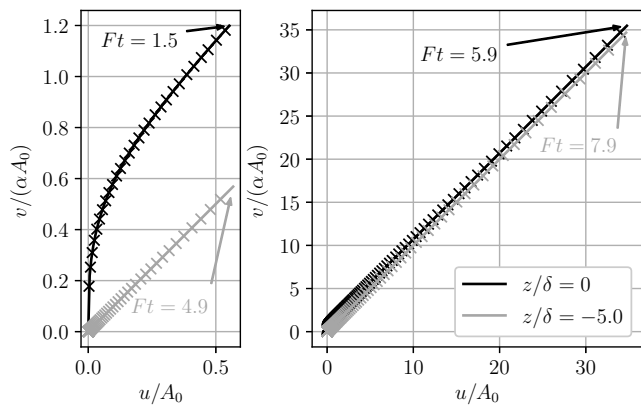


FIG. 5. Scaled hodographs at two different depths as time progresses. Left: short-term behavior. Right: long-term behavior. Annotated arrows indicate the time stamps on the last point of a given line. Solid lines are the theoretical prediction and crosses are the numerical simulation, with one cross displayed every time step. The axes are scaled equally, showing true angles in $(u, v/\alpha)$ coordinates.

In VI near the surface, V settles to a constant value, while U keeps growing quasi-exponentially (recall §II C). The near-surface velocity vector therefore adopts an angle of 45° with the mean flow in $u, v/\alpha$ coordinates (fig. 5, right panel). For $Z \ll -1$ however, $V \approx 0$ at all times, and the velocity vector adopts this 45° -angle immediately (fig. 5, $z = -5\delta$ lines).

We caution however on the analogy with ELs: the angle we just mentioned is with the direction of the *mean flow*, not that of the *wind direction*. Indeed, the appearance of this angle traces its roots back to eqns. (7), and to U and V being the solution of an unstable and stable partial differential equation, respectively. Incorporating a wind disturbance along x in EII would change $A(\tau)$, not the final orientation of the velocity vector.

C. Transport

Contrary to the EL case and its spiraling hodograph, the vertically integrated volume transport due to EII is mostly aligned with the direction of velocity field. When wind changes abruptly, we have, in EII coordinates,

$$\begin{bmatrix} M^{(U)} \\ M^{(V)} \end{bmatrix} = \delta \int_{-\infty}^0 \begin{bmatrix} U \\ V \end{bmatrix} dZ' = \frac{A_0 \delta}{2} \begin{bmatrix} e^\tau - 1 \\ 1 - e^{-\tau} \end{bmatrix}, \quad (19)$$

or, in across- and along-front coordinates,

$$\mathbf{M} = \begin{bmatrix} M^{(u)} \\ M^{(v)} \end{bmatrix} = A_0 \delta \begin{bmatrix} \cosh \tau - 1 \\ \alpha \sinh \tau \end{bmatrix}, \quad (20)$$

respectively. Also note that unlike σ_U , the growth rate of the mass transports reaches F quickly, i.e., over a duration of $O(F^{-1})$.

IV. DISCUSSIONS

A. Comparison with InI

While EII is similar to InI in several aspects, it also features several differences. For InI, $-LSP$ is the sole source of energy of the unstable perturbations. Velocities grow as part of spatially global modes, as opposed to the local (i.e., stress-driven) nature of EII expansion. In InI, the viscous flux divergence Φ_z and kinetic energy dissipation ε have passive roles, enhanced where InI creates stronger vertical shear, and decreasing the growth rate by a constant amount νm^2 , where m is the vertical wavenumber of the growing mode. Moreover, because $-LSP$ is not scale-selective, InI occurring in a comparable horizontally invariant domain tends to select larger scales to minimize the importance of viscous effects, while the vertical scale of the EII flow constantly increases with $\sqrt{\nu t}$.

Viscosity induces another major practical difference between InI and EII, namely that a large value of (eddy) viscosity can only prevent the former from growing, while it can aid the latter's expansion. Indeed, InI modes grow at a rate $F - \nu m^2$, and viscosity's only role is that of damping and scale selection. In EII, however, a larger viscosity has two consequences: (1) it speeds up the vertical propagation of EII via a larger δ , and (2) it decreases its magnitude since $A_0 \propto \nu^{-1/2}$. However, because EII grows fast during VIP, we can reasonably anticipate it to rapidly become detectable even in a highly turbulent environment, and to impart its signature at depth. Therefore, we argue that regardless of the value of eddy viscosity, EII is likely to always manifest itself, be it as an intense, near-surface current, or as a slower, slab-like motion of a significant vertical fraction of the front, or as some intermediate behavior.

One point of convergence between InI and EII refers to the 45° -angle in stretched coordinates between mean and EII flow. Recall that we cautioned in §III B against likening it to the surface deviation from the wind direction of the EL solution. On the other hand, a volume disturbance triggering InI would also induce flow that quickly aligns with the same angle as that of EII, by virtue of eqns. (7), which both EII and InI share.

B. Finite width of currents

As with all instabilities, EII induces a flow that will mix stable and unstable fluid, eventually extinguishing itself. Our solution does not include this effect because we kept Ro , i.e., ζ , constant, effectively providing an endless supply of unstable fluid. In an actual front however, ζ varies in space. In that case, $M^{(u)}$, the cross-jet volume flux induced by EII, will eventually provoke its extinction: the front is indeed surrounded by stable, $Ro > -1$ fluid, which would cap the unstable region and stop EII from growing any further.

Furthermore, EII will grow at different rates depending on the location within a front because Ro varies in space. As a consequence, a horizontal velocity divergence u_x will develop, compensated by a vertical velocity divergence w_z , a process called Ekman pumping for ELs. We can compute the vertical velocity w_∞ well below the region where EII occurs by vertically integrating the mass continuity equation, yielding $w_\infty = -M_x^{(u)}$. A comprehensive treatment of the corresponding “Ekman-inertial pumping” would require at least a two-dimensional study, and be further complicated by the fact that $\text{Ro} = O(1)$, meaning that x - and z -directions will be strongly coupled. We defer this study to future work.

V. CONCLUSIONS

Oceanic flows with anticyclonic vertical vorticity that over-compensates planetary vorticity (i.e., $\text{Ro} < -1$), are unstable to perturbations in surface boundary conditions. These perturbations rapidly propagate down via tangential viscous stress, at a rate that far supersedes that of InI, at least initially so, a regime we called “Viscous-Inertial Peeling”. After the instability is “primed” by the viscous stress however, the instability behaves like a slightly modified InI. In the simplest possible mathematical description we can make of it, namely, a columnar model, the vertical shear, compensated for inertial exponential growth, essentially follows a Rayleigh problem, and inherits its infinite initial growth rate. Assuming an abrupt change in wind conditions allowed us to write closed forms for the solutions, and therefore to make some of this behavior more explicit. After VIP, mass transport grows exponentially, at a rate F .

This instability not only shares several of its features with InI, its qualitative description inevitably brings up features, more common to an Ekman spiral, superposed with inertial oscillations. In fact, we mirror our derivation with that for the $\text{Ro} > -1$ case in the Appendix, which highlights striking similarities, and which prompted us to call this instability “Ekman-Inertial Instability”. In particular, the importance of viscous stresses, and the accompanying top-down propagation of momentum disturbances, is common to both, and provides EII with an initially infinite growth rate that may make it competitive with other instabilities such as InI, its baroclinic generalizations within the framework of centrifugal or symmetric instability, or baroclinic instability.

Whether this instability is novel or a mere flavor of InI is up for interpretation. More important however is to recognize EII’s peculiar behavior, which may manifest itself in peculiar ways in actual ocean fronts. Investigating more realistic, i.e., two- and three-dimensional configurations, will be the topic of future work. The points we raised in §III C would be a good start, which would inevitably raise new questions. In particular, how EII behaves in the presence of vertical and cross-jet buoy-

ancy variations promises interesting discussions. Our one-dimensional model can easily incorporate an evolution equation for the buoyancy b , namely,

$$b_t - u\bar{b}_x = \kappa b_{zz}, \quad (21)$$

where \bar{b} is the mean buoyancy field and κ is the buoyancy diffusivity coefficient. In our one-dimensional model still, b does not feed back into the momentum equations (2). Therefore, EII can advect water masses of different densities across the front, which could directly modify the potential energy of a density front. Grisouard [25] had observed that with similar boundary conditions, and contrary to predictions from symmetric instability theory, a horizontal flow was advecting buoyancy laterally immediately under the surface and extracting potential energy from the front. Moreover, minimal potential energy exchanges were found between front and fluctuations when the minimum anticyclonic Rossby number was large, which would have suppressed EII, and the Richardson number of the thermal wind shear was small, which would have favored symmetric instability. At the time, these behaviors had no complete explanations. In light of our results however, they were consistent with EII out-competing symmetric instability whenever Ro was sufficiently anticyclonic.

Finally, stability of EII to along-jet and other three-dimensional disturbances such as convection, surface wave effects [26, 27] or non-traditional effects [28] should be investigated, along with a more complete description of the competition with the transient growth of centrifugal, symmetric and/or baroclinic instability [29].

ACKNOWLEDGMENTS

We acknowledge the support of the Natural Sciences and Engineering Research Council of Canada (NSERC) [RGPIN-2015-03684], and of the Canadian Space Agency [14SUSWOTTO]. NG acknowledges fruitful discussions with James C. McWilliams, which originated during the Kavli Institute of Theoretical Physics program on Planetary Boundary Layers in Atmospheres, Oceans, and Ice on Earth and Moons (supported by the National Science Foundation under Grant No. NSF PHY-1748958), and with Francis Poulin.

Appendix: Comparison with the establishment of an Ekman spiral

When $\text{Ro} > -1$, re-defining $F = \beta f$, with $\beta = \sqrt{1 + \text{Ro}}$, better reveals the set-up of an EL. In doing so, eqns. (6)–(7) apply, albeit with the new definition of F . Note that we do not need to solve for both U and V anymore, since u and v derive from the real and imaginary parts of either of them. In line with the traditional presentation of ELs, we solve for $\tilde{V} = u + iv/\beta$ and introduce the counter-rotated field $\tilde{V}^\ddagger = \tilde{V}e^{i\tau}$ to obtain the

same diffusion equations such as the one in (8), and the counter-rotated boundary condition $\tilde{V}_Z^\dagger|_{Z=0} = iA(\tau)e^{i\tau}$, with $A = v_z|_{z=0}/\beta$. The solution is formally identical to eqn. (11), with the exception of $ie^{-i\theta}$ replacing $e^{-\theta}$. When surface boundary conditions change abruptly,

$$\tilde{V} = \frac{A_0 e^{i\pi/4}}{2\sqrt{2}} \left[e^{Z\sqrt{2i}} \operatorname{erfc} \left(-\sqrt{i\tau} - \frac{Z}{\sqrt{2\tau}} \right) - e^{-Z\sqrt{2i}} \operatorname{erfc} \left(\sqrt{i\tau} - \frac{Z}{\sqrt{2\tau}} \right) \right]. \quad (\text{A.1})$$

As $\tau \rightarrow \infty$, $\tilde{V} \rightarrow A_0 e^{Z+i(\pi/4+Z)}/\sqrt{2}$, which is the classical Ekman spiral solution. To obtain this result, we used the identities

$$\frac{e^{i\pi/4}}{\sqrt{2}} \operatorname{erf}(\sqrt{i\tau}) = S(\sqrt{\hat{\tau}}) + iC(\sqrt{\hat{\tau}}) \rightarrow \frac{1+i}{2}, \quad (\text{A.2})$$

where S and C are the normalized Fresnel integrals, $\hat{\tau} = 2\tau/\pi$, and the last arrow implies $\lim_{\hat{\tau} \rightarrow \infty}$.

At the surface,

$$\tilde{V}|_{Z=0} = A_0 \left[S(\sqrt{\hat{\tau}}) + iC(\sqrt{\hat{\tau}}) \right]. \quad (\text{A.3})$$

For $\tau \ll 1$, $C(\sqrt{\hat{\tau}}) \approx \sqrt{\hat{\tau}}$, i.e., exhibits a growth rate singularity, similar to that of EII. In the other limit $\tau \gg 1$, $C(\sqrt{\hat{\tau}}) - 1/2 \approx \sin \tau / \sqrt{2\pi\tau}$, with S behaving similarly. That is, the convergence to the EL solution manifests itself as near-inertial, or near- F frequency, pseudo-oscillations. Note that their envelope decays as $1/\sqrt{2\pi\tau}$, identical to that of $\sqrt{2/\pi}D(\sqrt{\tau})$, the compensated EII magnitude. The time evolution of the surface hodograph resembles that of a Cornu spiral, albeit one that converges more slowly towards its attractor and with a constant quasi-frequency F .

Like EII, this solution highlights two phases: first, that of a rapid adjustment (singular growth rate), followed by a slow ($\sim \tau^{-1/2}$) and oscillatory convergence towards constant values $u/A_0 = v/(\beta A_0) = -1/2$, which is the surface expression of the EL. These two phases are of course the stable counterparts to EII's VIP and InVI stages. In fact, because we defined VIP as the phase during which rotation has not affected the motion yet, it appears natural that VIP is shared by both EII and EL.

Contrary to EII however, a wind disturbance of arbitrary orientation corresponds to a surface boundary condition for \tilde{V}_z that is not purely imaginary, and whose phase encodes the disturbance direction. As a result, the orientation of u and v is with respect to the *wind direction*, not the *mean flow*.

-
- [1] G. K. Vallis, *Atmospheric and Oceanic Fluid Dynamics* (Cambridge University Press, Cambridge, 2017).
- [2] V. W. Ekman, On the influence of the earth's rotation on ocean-currents., *Arkiv för Matematik, Astronomi och Fysik* **2**, 1 (1905).
- [3] J. O. Wenegrat and L. N. Thomas, Ekman transport in balanced currents with curvature, *Journal of Physical Oceanography* **47**, 1189 (2017).
- [4] M. E. Stern, Interaction of a uniform wind stress with a geostrophic vortex, *Deep Sea Research and Oceanographic Abstracts* **12**, 355 (1965).
- [5] P. P. Niiler, On the Ekman divergence in an oceanic jet, *Journal of Geophysical Research* **74**, 7048 (1969).
- [6] Y. Morel and L. N. Thomas, Ekman drift and vortical structures, *Ocean Modelling* **27**, 185 (2009).
- [7] D. G. Dritschel, N. Paldor, and A. Constantin, The Ekman spiral for piecewise-uniform diffusivity, *Ocean Science Discussions in review*, 10.5194/os-2020-31 (2020).
- [8] V. I. Shrira and R. B. Almelah, Upper-ocean Ekman current dynamics: a new perspective, *Journal of Fluid Mechanics* **887**, A24 (2020).
- [9] L. N. Thomas, A. Tandon, and A. Mahadevan, Submesoscale processes and dynamics, in *Ocean Modeling in an Eddy Regime*, Geophysical Monograph Series, Vol. 177, edited by M. W. Hecht and H. Hasumi (American Geophysical Union, Washington, D. C., 2008) pp. 17–38.
- [10] J. C. McWilliams, Submesoscale currents in the ocean, *Proceedings of the Royal Society A: Mathematical, Physical and Engineering Science* **472**, 20160117 (2016).
- [11] A strict definition of submesoscale flows would also include a Richardson number that is order one, i.e., vertical geostrophic velocity gradients that are comparable to the buoyancy frequency of the density stratification. However, we will mostly ignore such effects.
- [12] P. Klein and G. Lapeyre, The Oceanic Vertical Pump Induced by Mesoscale and Submesoscale Turbulence, *Annual Review of Marine Science* **1**, 351 (2009).
- [13] M. Lévy, P. J. S. Franks, and K. S. Smith, The role of submesoscale currents in structuring marine ecosystems, *Nature Communications* **9**, 4758 (2018).
- [14] A. de Verneil, P. J. S. Franks, and M. D. Ohman, Frontogenesis and the creation of fine-scale vertical phytoplankton structure, *Journal of Geophysical Research: Oceans*, 2018JC014645 (2019).
- [15] J. O. Wenegrat, L. N. Thomas, J. Gula, and J. C. McWilliams, Effects of the submesoscale on the potential vorticity budget of Ocean Mode Waters, *Journal of Physical Oceanography* **48**, 2141 (2018).
- [16] Z. Su, J. Wang, P. Klein, A. F. Thompson, and D. Menemenlis, Ocean submesoscales as a key component of the global heat budget, *Nature Communications* **9**, 775 (2018).
- [17] R. Ferrari and C. Wunsch, Ocean Circulation Kinetic Energy: Reservoirs, Sources, and Sinks, *Annual Review of Fluid Mechanics* **41**, 253 (2009).
- [18] J. C. McWilliams, E. Huckle, J.-H. Liang, and P. P. Sullivan, The Wavy Ekman Layer: Langmuir Circulations, Breaking Waves, and Reynolds Stress, *Journal of Physical Oceanography* **42**, 1793 (2012).
- [19] J. C. McWilliams, J. Gula, M. J. Molemaker, L. Renault, and A. F. Shchepetkin, Filament Frontogenesis by Boundary Layer Turbulence, *Journal of Physical*

- Oceanography **45**, 1988 (2015).
- [20] M. N. Crowe and J. R. Taylor, The evolution of a front in turbulent thermal wind balance. Part 1. Theory, *Journal of Fluid Mechanics* **850**, 179 (2018).
- [21] T. W. N. Haine and J. Marshall, Gravitational, Symmetric, and Baroclinic Instability of the Ocean Mixed Layer, *Journal of Physical Oceanography* **28**, 634 (1998).
- [22] B. Cushman-Roisin and J.-M. Beckers, *Introduction to Geophysical Fluid Dynamics*, 2nd ed. (Academic Press, 2011).
- [23] K. J. Burns, G. M. Vasil, J. S. Oishi, D. Lecoanet, and B. P. Brown, Dedalus: A flexible framework for numerical simulations with spectral methods, *Physical Review Research* **2**, 023068 (2020).
- [24] See supplemental material at <https://github.com/ngrisouard/Ekman-Inertial-Instability>.
- [25] N. Grisouard, Extraction of Potential Energy from Geostrophic Fronts by Inertial-Symmetric Instabilities, *Journal of Physical Oceanography* **48**, 1033 (2018).
- [26] J. C. McWilliams and B. Fox-Kemper, Oceanic wave-balanced surface fronts and filaments, *Journal of Fluid Mechanics* **730**, 464 (2013).
- [27] J. C. McWilliams, Surface wave effects on submesoscale fronts and filaments, *Journal of Fluid Mechanics* **843**, 479 (2018).
- [28] V. Zeitlin, Letter: Symmetric instability drastically changes upon inclusion of the full Coriolis force, *Physics of Fluids* **30**, 061701 (2018).
- [29] V. E. Zemskova, P.-Y. Passaggia, and B. L. White, Transient energy growth in the ageostrophic Eady model, *Journal of Fluid Mechanics* **885**, A29 (2020).